

## Research Paper

# High-temperature oxidation of carbon fiber and char by molecular dynamics simulation



Linyuan Shi (石临源), Marina Sessim, Michael R. Tonks, Simon R. Phillpot\*

Department of Materials Science and Engineering, University of Florida, Gainesville, FL, 32611, USA

## ARTICLE INFO

## Article history:

Received 29 March 2021

Received in revised form

13 September 2021

Accepted 16 September 2021

Available online 22 September 2021

## Keywords:

Molecular dynamics

Carbon fiber

Oxidation

## ABSTRACT

Reactive molecular dynamics (MD) simulations are performed to study the initial stage of the oxidation of carbon fiber and amorphous carbon char with atomic oxygen at temperatures ranging from 1000 K to 4500 K. The carbon fiber and amorphous carbon models are generated by kinetic Monte-Carlo and liquid quench methods, respectively. The species formed in the simulation are characterized and carbon monoxide is found to be the primary product in both systems. The oxidation results are analyzed in terms of the lifetime of molecules and the reaction rates of various species. Oxygen is found to be adsorbed on the surface of both carbon fiber and amorphous carbon char. Since the amorphous carbon has a significantly larger surface area, the number of oxygen atoms adsorbed on the amorphous carbon surface is significantly higher than on the carbon fiber surface. Six reaction models are proposed to fit the simulation results from which reaction rates at various temperatures are obtained. Reaction rates of the key reactions: carbon oxidation and oxygen adsorption follow the Arrhenius law and the activation energy is extracted for these reactions. These reaction rates are used to predict the long-time evolution of these systems.

© 2021 Elsevier Ltd. All rights reserved.

## 1. Introduction

Space vehicles experience extreme heating rates when entering a planetary atmosphere at extreme hypersonic speed. The temperature in the shock layer can be over the 10,000 K and the vehicle can experience a heat flux as high as 1 kW/cm<sup>2</sup> [1]. Therefore, a Thermal Protection System (TPS) is required to maintain the integrity of the spacecraft. In some systems, such as the US space shuttle and SpaceX's Crew Dragon capsule, thermal insulation is used. As an alternative, particularly for single use vehicles, ablative materials are used for thermal protection. While thermal insulation systems rely on the low thermal conductivity of the insulator to limit heat transport to the spacecraft, ablative heat shields rely on the consumption of heat in energetically expensive chemical reactions by low thermal conductivity ablative materials. Phenolic Impregnated Carbon Ablator (PICA) is a typical ablative material developed by NASA AMES research center that offers low thermal conductivity and efficient ablation properties [2] and has been successfully used in previous missions including Stardust Sample

Return Capsule [3], Mars Science Laboratory [4], Origins Spectral Interpretation Resource Identification Security - Regolith Explorer (OSIRIS-REX) [5] and Mars 2020 [6].

PICA is designed as a carbon fiber (CF) insulator with a phenolic resin binder. The high temperature of the shock layer created by the vehicle in the entry process not only makes PICA oxidize and/or pyrolyze to gaseous products and absorbs a large amount of heat in the ablation, but also dissociates the ambient atmospheric gases. Atomic oxygen is the most reactive species which diffuses through the boundary layer and reacts with the PICA for Earth and Mars entry, although molecular oxygen and atomic nitrogen is also important [7]. The phenolic resin matrix is converted to amorphous carbon and the CF surface is pitted in the pyrolysis process. The gases produced by the pyrolysis drive the chemical-reactive shock layer gases away from the spacecraft, providing additional thermal protection [8]. Moreover, the porous carbonaceous char pyrolyzed from the resin continually absorbs heat and reduces the conduction of heat into the interior of the PICA material; however, it can decompose through sublimation or be removed by spallation [9]. Thus, the oxidation of carbon (including both the CF and the char) is central to the ablation of PICA and other carbon-based TPS materials. However, since the gas-phase and gas-surface chemistry within the boundary layer in the ablation process is complicated, it

\* Corresponding author.

E-mail address: [sphil@mse.ufl.edu](mailto:sphil@mse.ufl.edu) (S.R. Phillpot).

is challenging to model the oxidation of CF and char under nonequilibrium and hypersonic conditions.

Modeling and simulation at various length scales has been applied to resin pyrolysis and carbon oxidation. Poovathingal et al. and Krishnan et al. [10,11] developed a finite-rate model for carbon surface oxidation using data from molecular beam experiments [12] to predict the reaction rates of O, CO, and CO<sub>2</sub> at various temperatures. Lachaud et al. [13,14] developed a multiscale model to investigate the oxidation of a carbon preform and oxidation of a char layer in the ablation process. In addition to macroscopic models, Molecular Dynamics (MD) simulation has also been employed to investigate the pyrolysis of resin. The initial stage of the carbonization of phenolic resin was investigated by Jiang et al. [15] using reactive MD. They identified H<sub>2</sub>O is the first reaction product and observed other small species such as H<sub>2</sub>, CO, and C<sub>2</sub>H<sub>2</sub>. Bauschlicher and Qi et al. [16,17] simulated and compared the pyrolysis of phenolic resin with reactive force field (ReaxFF) simulations, density-functional tight-binding (DFTB), and density functional theory (DFT) modeling methods. They also identified the reaction paths associated with the production of CO, H<sub>2</sub>, and H<sub>2</sub>O. Desai et al. [18] used carbon nanotube and graphene layers to represent the CF and investigated its effect on the pyrolysis of resin and found that they have essentially no effect on the pyrolysis process. MD simulations by Poovathingal et al. [19] showed that there is no carbon removal from pristine highly-oriented pyrolytic graphite even when ion irradiated with the 5 eV atomic oxygen. Both of these results for irradiation of graphene layer and nanotube results are consistent with the high energy barrier for the removal of carbon from a perfect graphene layer. Poovathingal et al. [19] also found that pre-existing defects in the CF reduce the energy barrier and lead to increased carbon removal, followed by the rapid growth of an etch pit. The real fiber has a much more complicated structure than the pristine graphite, with graphitic sheets arranged to form radial, random, onionskin, skin-core or hollow porous structures depending on the precursors and processing methods [20].

Since CFs also have many pores, defects and sp-coordinated dangling bonds [21,22], carbon atom removal in the oxidation process is likely much easier than seen in MD simulations of graphitic sheets. However, there has been little work on modeling the oxidation process of CF and char at the atomic scale due to their complex structure. Recently, several new atomic CF models have been proposed and have made it possible to perform reactive MD oxidation simulations. Desai et al. [23] developed a molecular model to generate CF microstructure from small ladder-like molecules by combining kinetic Monte Carlo (kMC) and MD techniques. Desai's model was improved upon by Shi et al. [24] using a virtual energy wall to create a CF with a well-defined surface. Ranganathan et al. [25] developed and characterized amorphous carbon at a wide range of densities from 0.5 g/cm<sup>3</sup> to 3.2 g/cm<sup>3</sup> using a liquid quench method. He et al. [26] developed a nanofiber model with a heterogeneous microstructure, which can model the skin-core features of CF. These new, high-fidelity, CF and amorphous carbon models provide an opportunity to model the oxidation process and to investigate the reaction process during pyrolysis at the atomic scale.

The present work focuses on modeling the reaction processes between atomic oxygen and CF/char at high temperatures and characterizes the key kinetic properties, including activation energy of reactions and reaction products. This article is organized as follows: Sections 2.1 and 2.2 briefly introduce the generation method of the CF and amorphous carbon char models. Section 2.3 details the overall setting of the MD simulation initialization and characterization methodology. Section 2.4 shows the prediction model of oxidation based on MD simulation. Section 2.5 discusses how to characterize the adsorbed oxygen atom on the surface of CF

and amorphous carbon. Section 3 presents the simulation results and predictions of the oxidation process of CF and char. Section 4 contains our conclusions.

## 2. Computational methods

### 2.1. Generation of the carbon fiber structure

The high-fidelity CF microstructure is generated by the combined kMC and MD method developed by Desai et al. [23] and refined in our previous work [24]. This kMC-MD approach lends itself well to model CFs that have complex cross-sectional structures. We have used this method to generate two types of CF models, fiber cores and thin fibers, at a wide range of densities. Compared with other high-fidelity CF models [27,28], the advantage of this kMC-MD method is that it can generate a CF microstructure with a well-defined surface, a capability that is exploited in the thin fibers. Such a thin fiber model is employed in this work for CF oxidation.

The full synthesis method is described elsewhere [24], but briefly summarized here for completeness. The overall steps in the generation process are: (1) pack aligned eight-carbon atom ladder units at random positions in a simulation cell that is very thin along the z-axis, (2) equilibrate the whole system at 300 K for 25 ps, (3) run the kMC-MD bond formation cycle for 360 iteration loops to ensure the graphitization of the CF, (4) replicate the quasi-2D microstructure along the z-axis to obtain a full 3D structure, and (5) equilibrate the thin fiber structure at 300 K for 10 ps. For the generation of a thin fiber, during the initial generation of the microstructure, the structural units are constrained within a cylindrical region by a virtual energy wall; this results in a well-defined surface. All key parameters in the generation process are the same as in our previous work [24] except the initial system size. In order to capture more oxidation reactions, the current CF model is larger than it in the previous work. In this work, 61,704 carbon atoms are packed in a thin cylindrical region with a 1.92 g/cm<sup>3</sup> initial density. The initial diameter of the fiber is 400 Å, as imposed by the virtual energy wall. In step 4 above, the quasi 2D structure is replicated 10 times to generate full 3D structure; the system thus contains 617,040 carbon atoms after replication. This CF model's dimensions are 772 × 782 × 50 Å<sup>3</sup> after the equilibration in step 5. The detailed characterization of this fiber model include chemical bonding and comparison with the experimental results can be found in our previous work [24].

### 2.2. Generation of the amorphous carbon char structures

The amorphous char structure used in this study is generated using the liquid quench method developed by Raghavan et al. [25]. The overall steps are: (1) place N carbon atoms at random positions in the fully periodic simulation cell at constant volume and heat to 10,000 K, (2) equilibrate the system at 10,000 K for 15 ps, (3) quench the system to 3000 K at a quench rate of 50 K/ps (4) anneal the system at 3000 K for 140 ps, (5) quench the system to 300K, again at 50 K/ps, and (6) anneal the system at 300K with constant volume (NVT) and constant pressure (NPT) for 10 ps respectively. This model mimics a gas phase under high temperature equilibration followed by quenching and annealing to form an amorphous carbon microstructure. The time step is 0.07 fs in the generation process, as in Raghavan's work. More details about this method and the characterization of the amorphous structure can be found in Raghavan's paper [25]. Since Lachaud et al. [14] modeled the ablation process of the PICA by a macroscopic approach and found the density of the char layer after the ablation to be 0.2–0.3 g/cm<sup>3</sup>, the initial density of this amorphous carbon char is

set to  $0.3 \text{ g/cm}^3$ ; there are 150,000 carbon atoms in the system. The char model's dimensions are  $215.4 \times 215.4 \times 215.4 \text{ \AA}^3$  after the NVT and NPT equilibration in step 6. Moreover, we find that not all carbon atoms condense into the amorphous carbon char structure; there are thus some small carbon species, such as  $\text{C}_2$ ,  $\text{C}_3$ , in the structure. Since most of carbon atoms in these species are unsaturated with many dangling bonds, these species are very reactive with oxygen atoms. To avoid the spurious influence of these small species on our results, molecules that have less than 10 carbon atoms are identified and removed from the system prior to the oxidation simulation. In Fig. 1(a) 1070 out of 150,000 carbon atoms are identified as being in such small clusters and colored as bright green; removing these atoms only decreases the number of atoms in the system by 0.7%. Fig. 1(b) shows the amorphous carbon char structure with these atoms removed; this is the initial structure prior to the oxidation simulation. Compared with the initial density  $0.3 \text{ g/cm}^3$ , the current density of the amorphous carbon structure is  $0.297 \text{ g/cm}^3$  after the removal of the unsaturated small molecules, which is still within the range obtained by Lachaud et al. [14]. Moreover, the surface area of this char model is  $899 \text{ m}^2/\text{g}$ , which is of the same order as the experimental surface area of the low heating rate char ( $588 \text{ m}^2/\text{g}$ ) [29]. The fundamental difference between fiber and char is that char is a highly interconnected  $\text{sp}^2$  network. The percentages of  $\text{sp}^2/\text{sp}^3$  for fiber and char are 6.3%/93.6%/0.1% and 8.1%/89.6%/2.3%, respectively. Thus, compared with the fiber, char has a slightly higher percentage of  $\text{sp}$  and  $\text{sp}^3$  hybridized carbon atoms. The interconnected structure, large voids that allow rapid diffusion of atomic and other gases, and large surface area are the key characteristics of char.

### 2.3. Overall simulation settings

The LAMMPS software [30] is used for all microstructure generation and oxidation simulations presented in this work. During the relaxation of the initial structure and bond formation process (steps 1–3) of the generation of CF, the computationally efficient Dreiding force field [31] is employed to describe the covalent atomic interactions, while the Lennard Jones (LJ) potential is employed to describe the van der Waals interactions. The *Moltemplate* package [32] is used to attach the Dreiding force field and bonding information to the coordination files. In step 5 of the generation of the CF model, and in all subsequent steps and the oxidation simulations of the CF and amorphous char, the more physically realistic ReaxFF (reactive force field) [33] potential is used for both models; this force field has been successfully used to model the pyrolysis of phenolic resin [34] and various novel

carbon-like structures, including graphene oxide [35] and carbon nanotubes [36]. Moreover, ReaxFF allows dynamic bond breakage and formation by using the concept of bond order within a reactive system.

The *Ovito* software [37] and its Python interface are used to visualize the simulations and to analyze the results of the oxidation simulation. The *Packmol* package [38] is used for insertion of structural units in the CF generation process and insertion of oxygen atoms in the oxidation models. In order to make the oxidation of the CF and char simulation comparable, the initial concentration of oxygen atom is set to  $0.5 \text{ mol/L}$  in both models. It should be noted that to increase the chance of reaction and accelerate the oxidation simulation process, the oxygen concentration in this work is much higher than in the atmosphere and mesosphere. Since, as we shall see, the oxidation process primarily involves the oxidation of single carbon atoms to form CO, this high pressure does not introduce chemical reactions absent at low pressures; it merely, increases the reaction rate without changing the overall kinetics. The “Construct Surface Mesh” capability in *Ovito* is used to construct the polyhedral surface mesh around carbon atoms for analysis. For the surface mesh, the probe radius is set to  $8 \text{ \AA}$  and the smoothing level is also set to 8 iterations of the smoothing algorithms for both fiber and char. Although the shape is irregular, the actual occupied volume of generated CF and char models can be accurately obtained from the enclosed area using this method. Fig. 2(a–b) show the generated CF and amorphous char models with the surface meshes colored as translucent bright green. To initialize the oxidation simulations, 7893 (for CF) and 2548 (for char) oxygen atoms are packed into the empty space of the simulation cell, as shown in Fig. 2(c–d). Since the ReaxFF potential uses bond order to determine if two atoms are bond with each other, the minimal distance tolerance between one oxygen atom and the other atoms is set to  $2 \text{ \AA}$  to avoid oxygen–oxygen bond formation during the packing process and energy minimization.

After oxygen atoms insertion, the oxidation of CF and amorphous char systems are simulated in the following steps: (1) relax the initial system by energy minimization with the conjugate gradient algorithm, (2) equilibrate the system at the zero pressure and at  $300 \text{ K}$  for  $10 \text{ ps}$ , and (3) rescale the temperature to the target temperature  $T$  with the canonical ensemble (NVT) for  $90 \text{ ps}$  to simulate the initial stage of the oxidation process. To investigate the influence of the temperature on the oxidation process, the target temperature  $T$  in each simulation is set from  $1000 \text{ K}$  to  $4000 \text{ K}$  in  $500 \text{ K}$  intervals. Moreover, we find that the simulation cell of CF model slightly shrinks after equilibration in the steps 1 and 2, slightly increasing the initial oxygen concentration in the CF

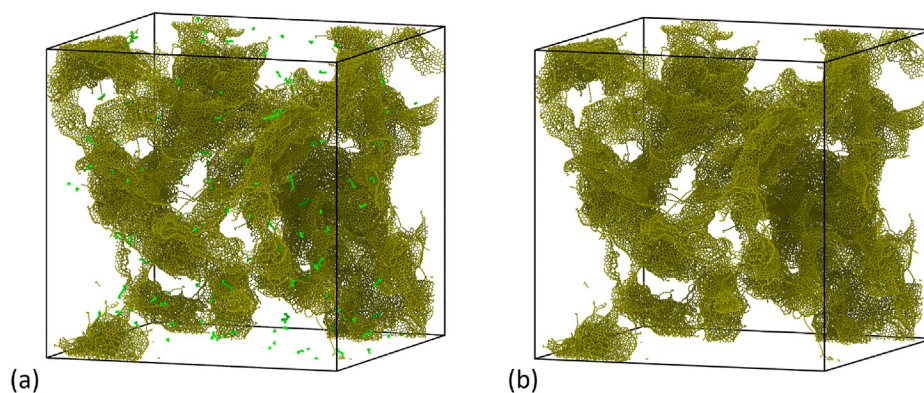


**Fig. 1.** (a) The carbon char model before the removal of the carbon atoms in the small clusters. (b) The carbon char model after the removal of the carbon atoms in the small clusters. Carbon atoms in the small clusters are intentionally enlarged and colored as bright green. Carbon atoms in the char are colored as darker green. (A colour version of this figure can be viewed online.)

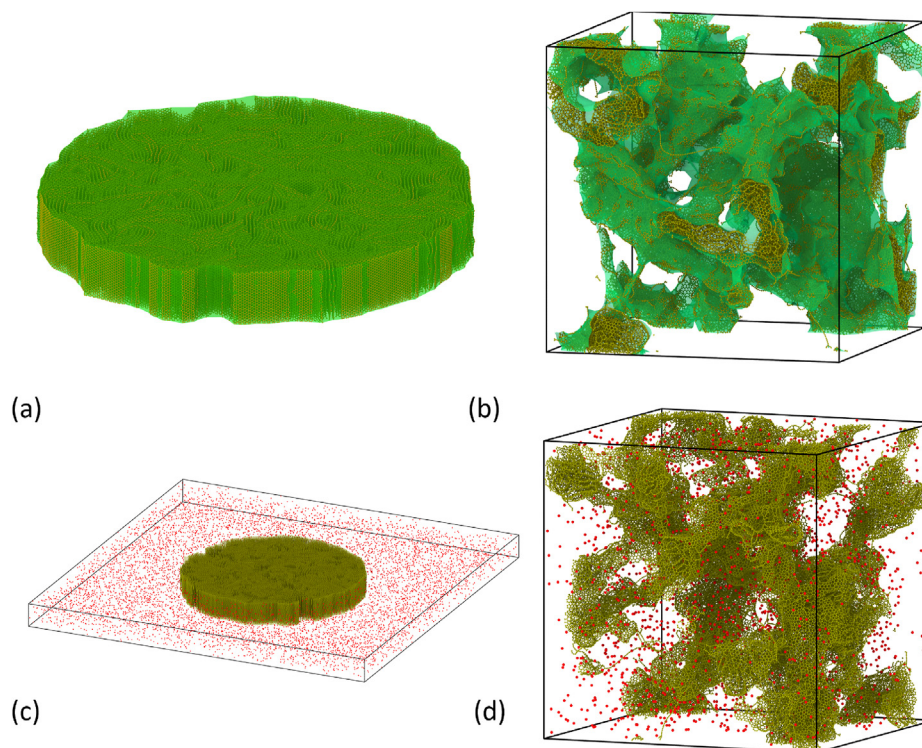


**Fig. 2.** (a) 3D view of the generated CF model with the surface mesh. The simulation cell is hidden for a better view. (b) 3D view of the generated amorphous carbon char model with the surface mesh. (c–d) The oxidation models of CF and amorphous carbon char after oxygen atoms insertion. The carbon atoms are colored as green. The surface mesh area is colored as translucent bright green in (a–b). Oxygen atoms are colored as red in (c–d). (A colour version of this figure can be viewed online.)

simulation to 0.53 mol/L. In addition, although the simulation cell of the amorphous carbon char doesn't shrink during the equilibration, we observe that many oxygen atoms are adsorbed onto the surface of the amorphous char due to the large surface area. Therefore, the initial free oxygen concentration in the amorphous carbon char model decreases to 0.46 mol/L after equilibration. Periodic boundary conditions are applied, and the time step is 0.1 fs in the oxidation simulation. The analysis of the species is performed with a 1.8 Å cutoff for all atom pairs to determine if bond forms between atoms. The molecular species present are inventoried every 10 fs. These data provide detailed information for the analysis of the initial stage of the oxidation.

#### 2.4. Reaction parameter analysis

The dynamic snapshots of MD simulation contain detailed information of the trajectory of all atoms. Therefore, every atom that makes up each molecule can be tracked. By tracing the path of each atom through its various bonding environments, the lifetime of each species can be identified and counted separately. Since the true lifetime of any gaseous species that is present at the end of the simulation cannot be determined, they are not considered in the lifetime calculations.

The CF-oxygen and char-oxygen reaction mechanism is fairly complicated. It is beyond the scope of this paper to take account all the factors that influence the initial stage of oxidation of CF and char. A necessary and sufficient oxidation mechanism is described here based on Poovathingal's model [10], where he uses finite-rate gas–surface reaction models to predict macroscopic behavior of CF oxidation such as mass loss rates and rate parameters. As shown in Table 1, we consider several possible reaction mechanisms and analyze six oxidation models. The complexity of each model is determined by the number of specific chemical reactions that are

included in the analysis. In all of these models, we assume that all reactions are first order reactions and that the rate is only related to the instantaneous concentration of reactants. Based on Poovathingal's model and our findings in Section 2.5, oxygen atoms can be adsorbed and desorbed on the empty sites of the surface of CF and carbon char where carbon atoms have dangling bonds.

Reactions 1 and 2 in Table 1 account for the reversible oxygen adsorption/desorption mechanism, where (s), O and  $O_s$  are an empty site on the carbon matrix, atomic oxygen and surface-adsorbed oxygen atoms respectively. Reactions 3 and 4 describe the reaction of carbon atoms in CF/char with the atomic and adsorbed oxygen atom to generate CO respectively. Although the initial large separation of atomic oxygen atoms means that there is little formation of oxygen molecules during the equilibration, it is possible for oxygen molecules to be generated during the oxidation simulation at high temperature. This mechanism is described in reaction 5. Reaction 6 is the dissociative adsorption of the  $O_2$ , where one of the O atoms from the  $O_2$  molecules adsorbs on an empty carbon site. Reaction 7 describes the possible dissociative adsorption of  $CO_2$ , where one of the O atoms from the  $CO_2$  molecule adsorbs on an empty carbon site. Reactions 8 through 12 describe several possible reaction paths to generate CO or  $CO_2$ . We also find some small molecular species products generated in the oxidation simulation (see discussions in Sections 3.1 and 3.2). Thus, reactions 13 and 14 account for the generation of these small species, represented as  $C_xO$ ; most of these are actually  $C_2O$ . In reaction 15, used only in model 2, the atomic and adsorbed oxygen atoms are treated as a single entity for oxidation of the CF or char.

Since the number of oxygen atom in the  $C_xO$  species is fairly small (no more than 3% of the total number of oxygen atoms), for simplicity they are not considered separately in models 1–5 but treated as part of  $O_s$ . For these models, the number of  $O_s$  is calculated by subtracting the number of oxygen atoms in O,  $O_2$ , CO and

**Table 1**  
Reaction rate fitting models.

Mechanisms	Rate	Model 1	Model 2	Model 3	Model 4	Model 5	Model 6
1) $O + (s) \rightarrow O_s$	$k_1[O]$	✓	✓	✓	✓	✓	✓
2) $O_s \rightarrow O + (s)$	$k_2[O_s]$	✓	✓	✓	✓	✓	✓
3) $C + O \rightarrow CO$	$k_3[O]$	✓		✓	✓	✓	✓
4) $C + O_s \rightarrow CO$	$k_4[O_s]$			✓	✓	✓	✓
5) $O + O \rightarrow O_2$	$k_5[O][O]$				✓	✓	✓
6) $O_2 \rightarrow O + O_s$	$k_6[O_2]$				✓	✓	✓
7) $CO_2 \rightarrow CO + O_s$	$k_7[CO_2]$				✓	✓	✓
8) $C + 2O \rightarrow CO_2$	$k_8[O][O]$				✓	✓	✓
9) $2C + O_2 \rightarrow 2CO$	$k_9[O_2]$					✓	✓
10) $CO + O \rightarrow CO_2$	$k_{10}[CO][O]$					✓	✓
11) $C + O_2 \rightarrow CO_2$	$k_{11}[O_2]$					✓	✓
12) $CO_2 + C \rightarrow 2CO$	$k_{12}[CO_2]$					✓	✓
13) $C_x + O \rightarrow C_xO$	$k_{13}[O]$						✓
14) $C_x + O_s \rightarrow C_xO$	$k_{14}[O_s]$						✓
15) $C + O/O_s \rightarrow CO$	$k_{15}[O/O_s]$		✓				

$CO_2$  from the total number of the oxygen atoms in the system. The  $O_s$  and  $C_xO$  are separately considered in model 6, where the number of  $O_s$  is counted based on the method described in section 2.5. The number of  $C_xO$  is calculated by subtracting the number of oxygen atoms in  $O$ ,  $O_s$ ,  $O_2$ ,  $CO$  and  $CO_2$  from the total number of the oxygen atoms. Each reaction has a corresponding reaction rate; for example, the adsorption rate from reaction equation (1) is  $k_1[O]$  where  $k_1$  is the temperature-dependent reaction constant and  $[O]$  is the concentration of oxygen atoms. The rate of this reaction can also be expressed as:

$$\frac{d[O_s]}{dt} = k_1[O] \quad (1)$$

Therefore, the ordinary differential equations in the models can be combined together and rewritten as a system of ordinary equations. For example, the rate of  $O$  consumption and  $CO$  generation in model 3 can be rewritten as:

$$\frac{d[O]}{dt} = -k_1[O] + k_2[O] - k_3[O] \quad (2)$$

$$\frac{d[CO]}{dt} = k_3[O] + k_4[O_s] \quad (3)$$

Since the evolution of the concentration of species as a function of time is obtained from the MD simulations, the slopes of the curve are the instant reaction rates. Therefore, this system of ordinary differential equations transforms to a system of linear equations. These linear equations are fitted to the simulation data to get the rate coefficients. To demonstrate this fitting approach, Fig. 3 compares the fitted time dependence of the concentration of species calculated by model 6 with the actual concentrations obtained from the oxidation simulation of CF at 3500 K. Similar curves were generated using the six models at all simulated temperatures. The activation energy  $E_a$  and the pre-exponential factor  $A$  can be obtained by fitting reaction constants in the linearized Arrhenius law:

$$\ln(k) = \ln(A) - \frac{E_a}{RT} \quad (4)$$

where  $R$  and  $T$  are the ideal gas constant and temperature, respectively. The error of the fitted model is calculated by:

$$error = \frac{1}{K} \frac{1}{N} \frac{1}{M} \sum_{k=1}^K \sum_{j=1}^N \sum_{i=1}^M \frac{2|x_{ijk} - x'_{ijk}|}{|x_{ijk} + x'_{ijk}|} \quad (5)$$

where  $x_{ijk}$  and  $x'_{ijk}$  are the concentrations of the species from the simulation and model prediction results of the  $i_{th}$  sample point at the  $j_{th}$  temperature for the  $k_{th}$  species in the simulation, respectively. Since each model fits several species concentration curves as the function of time at different temperatures, the error is averaged by the number of fitted curves  $K$ , the number of the simulations at the various temperatures  $N$ , and the number of sampling points  $M$ . Since the species curves of  $O$ ,  $CO$  and  $O_s$  are included in all models, only these species are considered in the error analysis. The error analysis and comparison between models will be discussed in Section 3.

Because the oxidation process is so complex, detailed analysis and advanced methods are needed in the post-processing of the data. In addition to analytic mathematical reaction models, there are other methods to analyze the oxidation process. In particular, since the snapshot contains the trajectory of every atom, it is possible to identify each individual reaction in the simulations. Then, the rate of each reaction can be computed by directly counting the number of individual reactions occurring in the simulation. Such an approach was previously successfully applied in the analysis of hydrogen peroxide decomposition [39]. However, unlike the hydrogen peroxide decomposition, separating individual reactions in this work is substantially more difficult since many individual reactions can occur on the surface of CF/char at the same time.

## 2.5. Oxygen adsorption on surface

During the oxidation, the main products observed are  $CO$ ,  $O_2$  and  $CO_2$ . Therefore, the primary processes of interest are their formation from the initial atomic oxygen atmosphere. As shown in Fig. 4(a), the fraction of initial oxygen atoms in four main gaseous species  $\frac{N_o + N_{co} + 2N_{o_2} + 2N_{co_2}}{N_{total}}$  is not conserved during the whole initial stage of the oxidation, where  $N_{total}$  is the total number of oxygen atoms in the system. However, since the total number of oxygen atoms  $N_{total}$  in the simulation is fixed, this indicates that additional processes are also taking place. We observed that almost all of the uncounted oxygen atoms are adsorbed on the surface of the carbon fiber, as evidenced by Fig. 4(c–d). The total number of oxygen

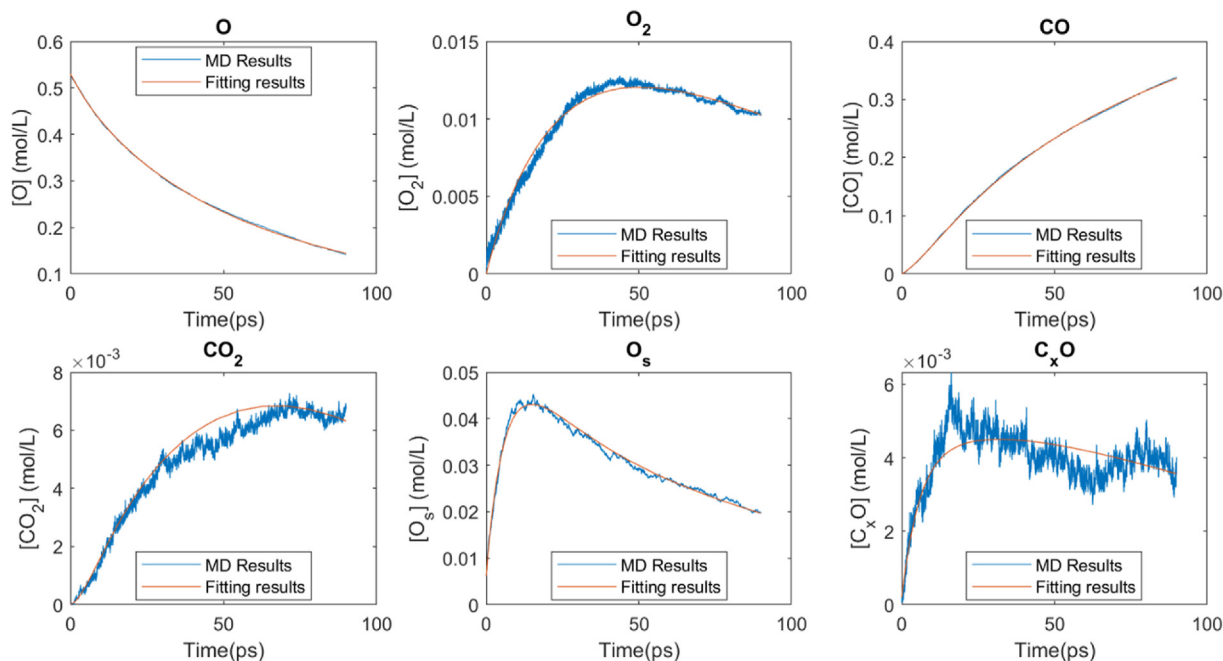


**Fig. 3.** Example of the model fitting; specifically, the predicted curve for the concentration of species fitted to model 6 (red curves) and the data obtained from the MD simulation (blue curves) from the oxidation simulation of CF at 3500K. (A colour version of this figure can be viewed online.)

atoms  $N_{total}$  can be refined as following:

$$N_{total} = N_O + N_{CO} + 2N_{O_2} + 2N_{CO_2} + N_{O(s)} + N_{C_xO} \quad (6)$$

where  $N_O$ ,  $N_{CO}$ ,  $N_{O_2}$ ,  $N_{CO_2}$ ,  $N_{O(s)}$  and  $N_{C_xO}$  are the number of O, CO,  $O_2$ ,  $CO_2$ ,  $O_s$  and  $C_xO$ , respectively. Because the carbon fiber is composed of many independent graphitic sheets, each sheet can be identified as an independent molecule  $C_m$  in the simulation, where  $m$  is the number of carbon atoms in the sheet. The graphitic sheets that adsorb oxygen atoms are identified as the  $C_mO_n$  where  $n$  is the number of oxygen atoms in the molecule. Compared with the small chemical species  $C'_mO'_n$ , a graphitic sheet has a very large value for  $m$  and a small value  $n$ . Therefore, the molecule  $C_mO_n$  is identified as a graphitic sheet with oxygen adsorption where  $m - n > 100$ ; the threshold value of 100 that determines whether the molecule is part of a graphitic sheet or is some other kind of species is somewhat arbitrary and was identified by trying various values and comparing the filtered results in the *Ovito* software. As shown in Fig. 4(b), after considering oxygen atom adsorption, the number of oxygen atoms accounted for by the four gaseous species and on the surface of fiber is more than 97% of the total number of oxygen atoms in the simulation at all temperatures. Moreover, we found that the main species in the remaining unaccounted-for molecules  $C_xO$  is  $C_2O$  with a very short lifetime due to its high reactivity. A detailed discussion about the lifetime of  $C_2O$  and other species will be presented in section 3.1. Fig. 4(c–d) and Fig. 4(e–f) show the direct evidence that oxygen atoms adsorbed on the surface of CF and amorphous carbon at different simulation times. The small molecules are intentionally hidden and only graphitic sheets or amorphous carbon meeting the above requirement are shown in these figures. Although the minimum distance between one oxygen atom and another atom (either C or O atom) is initially set to 2 Å to avoid the formation of unnecessary bonds, it is inevitable that few oxygen atoms adsorb on the surface of carbon and char during the energy minimization process as evidenced in Fig. 4(c) and (e).

### 3. Results and discussion

#### 3.1. Analysis of the oxidation of carbon fiber

As shown in Fig. 5(a), oxygen atoms have a relatively long lifetime at low temperature and a short lifetime at high temperature. With increasing temperature, oxygen atoms become more and more reactive and therefore the reaction rate increases, which lowers the average lifetime of oxygen. The concept of occurrence measures how often the species is generated and consumed. For example, if a particular oxygen atom appears as atomic oxygen at the beginning of the simulation, then reacts to be part of another species, which subsequently decomposes with products that include the atomic oxygen, then the occurrences for this oxygen atom as atomic oxygen is two. The occurrence of oxygen increases with increasing temperature, reaches a maximum at 3500 K and then decreases from 3500 K to 4500 K. We attribute the initial increase to a number of processes. First, with increasing temperature, atomic oxygen atom is more frequently adsorbed and desorbed from the surface of the carbon fiber surface. Second, a number of metastable species are generated in the MD simulation; because these metastable species are short lived, the atomic oxygen generated from the decomposition of the metastable species increases the number of its occurrences. It is interesting that the number of occurrences of atomic oxygen decreases between 3500 K and 4000 K. It seems that at these high temperatures many oxygen atoms react with the CF at the beginning of the simulation. Therefore, most of the CO is generated in the first half of the simulation. This consumes oxygen so quickly that both surface adsorption and generation of metastable species are largely suppressed.

As shown in Fig. 5(b), the average lifetime of  $O_2$  is fairly short compared with that of the atomic oxygen. However, unlike O, the average lifetime of  $O_2$  increases with the increase of temperature. The number of occurrences for oxygen molecules also increases from 1000 K to 2500 K and then decreases from 3000 K to 4500 K. The initial increase is due to the formation of molecules from the

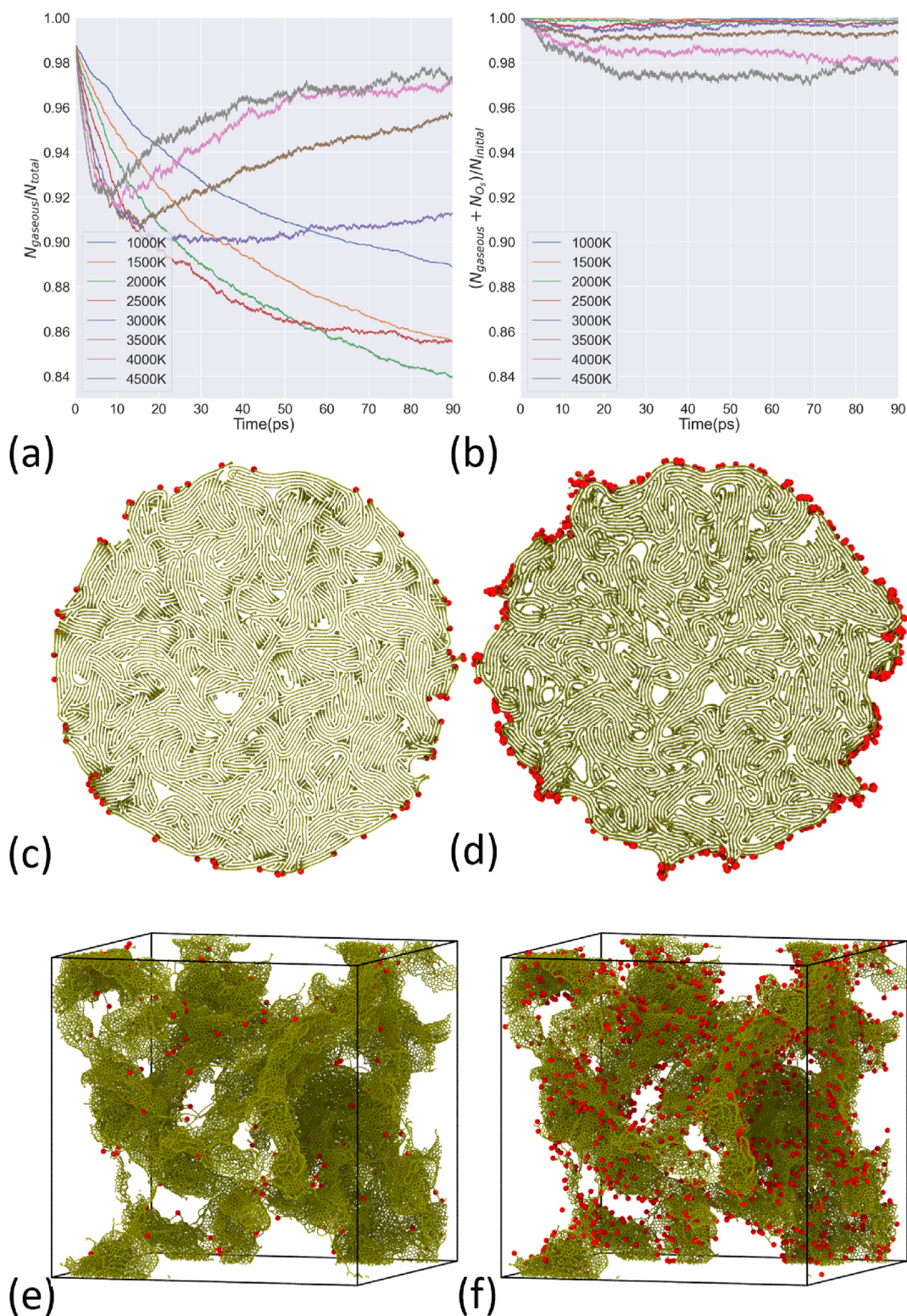


**Fig. 4.** (a) Total fraction of initial oxygen atoms in four main species O, O<sub>2</sub>, CO and CO<sub>2</sub> at different temperatures. (b) Total fraction of initial oxygen atoms in O, O<sub>2</sub>, CO and CO<sub>2</sub> and adsorbed on the fiber surface at different temperatures. (c–d) The snapshots of the initial state of the carbon fiber with adsorbed oxygen at the initial state and at 30 ps under 2000 K, respectively. (e–f) The snapshots of the initial state of the amorphous carbon char with adsorbed at the initial state and at 30 ps under 2500 K, respectively. Carbon and oxygen atoms are colored as green and red, respectively. The size of oxygen atoms is intentionally enlarged to make them easier to see. Only molecules identified as carbon in a graphitic sheet and adsorbed oxygen are kept in (c–f). (A colour version of this figure can be viewed online.)

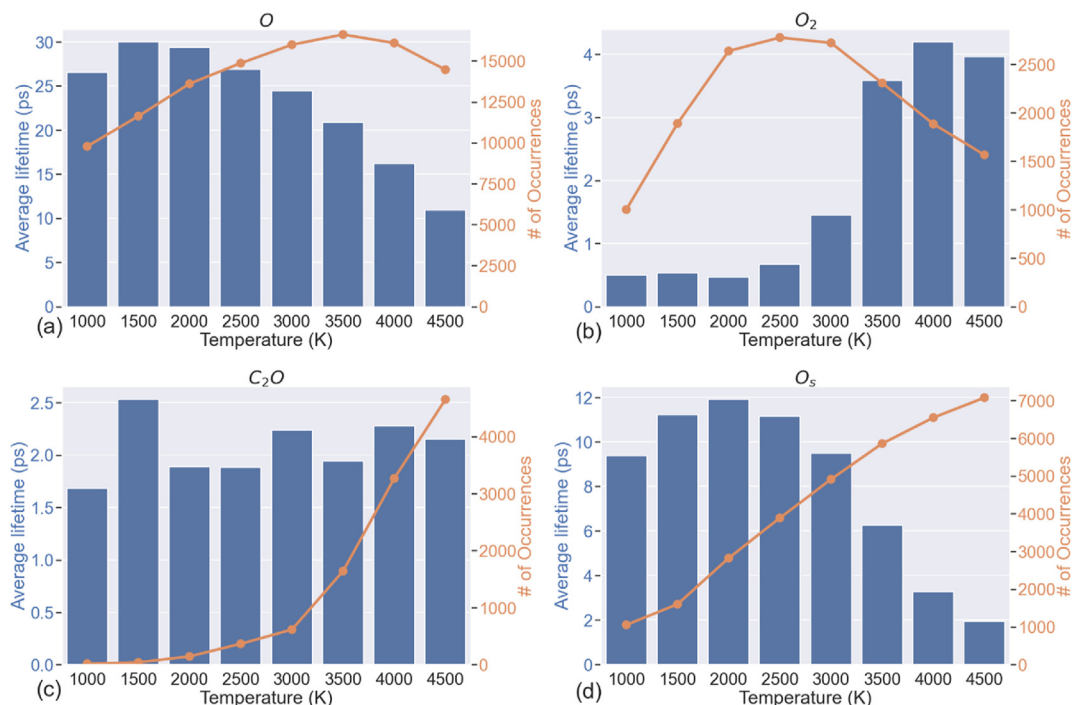


**Fig. 5.** (a–d) The average lifetime (blue bar) and occurrences (orange line) of O, O<sub>2</sub>, C<sub>2</sub>O and O<sub>s</sub> at from 1000 K to 4500 K during the oxidation simulation of CF. (A colour version of this figure can be viewed online.)

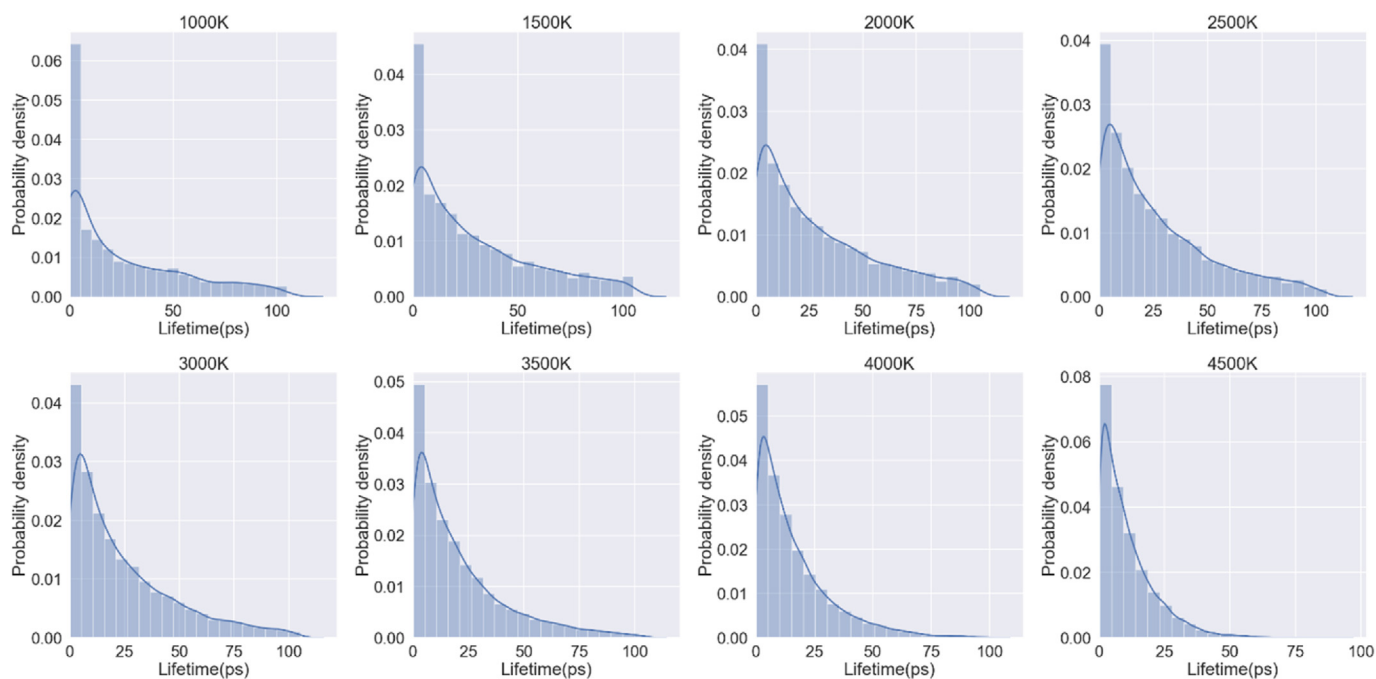


**Fig. 6.** The lifetime distribution of atomic oxygen at different temperatures from 1000 K to 4500 K and fitted by the gaussian kernel density estimation (blue line) for the carbon fiber oxidation. (A colour version of this figure can be viewed online.)

highly reactive atomic oxygen; the decrease is due to the rapid generation of CO at high temperature, which decreases the possibility of formation of O<sub>2</sub> since most of O are consumed for CO formation. As we discussed in section 2.5, the oxygen atoms in the four main gaseous species O, CO, O<sub>2</sub>, CO<sub>2</sub> and adsorbed oxygens O<sub>s</sub> account for more than 97% of the total oxygen atoms, the remaining 3% oxygen atoms mainly are in small molecules, mainly in the dicarbon monoxide (C<sub>2</sub>O) molecules, which is extremely reactive

and short lived. Indeed, as shown in Fig. 5(c), the lifetime of C<sub>2</sub>O less than 3 ps, indicative of its highly reactivity. This short lifetime of C<sub>2</sub>O may be one reason that it not observed in the experiment. The occurrence of C<sub>2</sub>O increases with increasing temperature, indicating that this molecule is frequently generated and then decomposes at high temperature. Fig. 5(d) shows that the average lifetime of O<sub>s</sub> decreases with the increasing temperature from 2000 K to 4500 K, indicating increasing reactivity. Also, the increase of

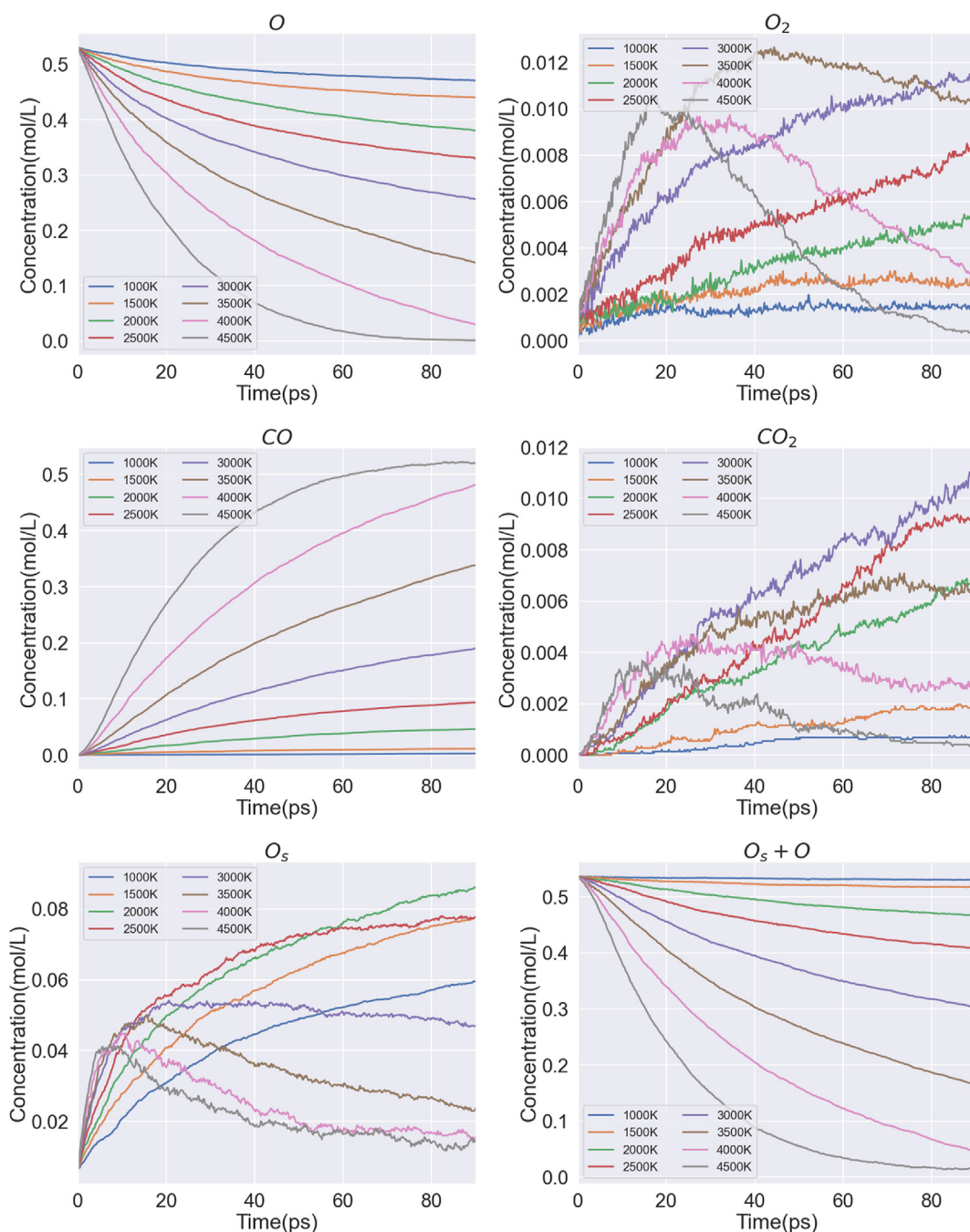


Fig. 7. The concentration of  $O$ ,  $O_2$ ,  $CO$ ,  $CO_2$ ,  $O_s$  and  $(O_s + O)$  as function of time during the oxidation simulations of carbon fiber. (A colour version of this figure can be viewed online.)

number of occurrences of  $O_s$  with increasing temperature shows that oxygen atoms are easier adsorbed on the fiber surface at high temperature but also quickly desorbed.

Fig. 6 shows the distribution of the lifetime of atomic oxygen as a function of temperature. These distributions are fitted by the gaussian kernel distribution estimation. Although the location of the peak of the distribution is almost independent of temperature, the range of the distribution shrinks with increasing temperature indicating increasing reactivity of atomic oxygen, corresponding well with the previous analysis of the average lifetime for atomic oxygen.

The concentration changes of the major species as function of time are shown in Fig. 7. It is unsurprising that the consumption

rate of atomic oxygen increases with increasing temperature, consistent with the higher reactivity at high temperature. The generation rate of molecular oxygen also increases with temperature. However, at high temperature the concentration of molecular oxygen decreases with time after the appearance of an initial peak. We attribute this decrease to decomposition to atomic oxygen at high temperature and the reaction of  $O_2$  to other species. It does however seem that molecular oxygen does not react with other species at low temperature; it is likely that this is due to the short simulation time,  $\sim 0.1$  ns, during which such reactions are rare. The rate of generation of  $CO$  increases significantly from 1000 K to 4500 K. The concentration of  $CO$  at 4500 K saturates with time because the oxidation process is now complete, with essentially all

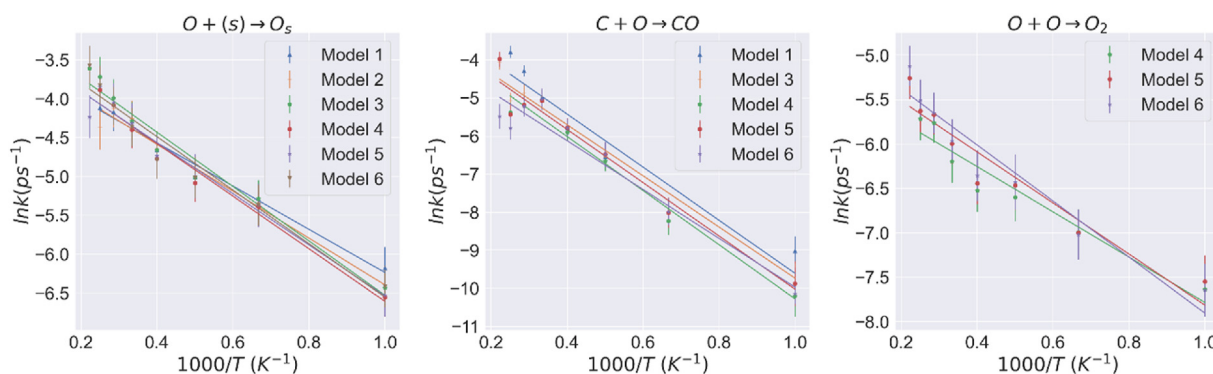


Fig. 8. Logarithm of the reaction rate against the inverse temperature for different reactions (a)  $O + (s) \rightarrow O_s$  (b)  $C + O \rightarrow CO$  (c)  $O + O \rightarrow O_2$  for the oxidation of CF.

Table 2

The activation energy of reactions fitted from Model 1 to Model 6 and the prediction error of each model for the oxidation of CF.

	$O + (s) \rightarrow O_s$ (kJ/mol)	$C + O \rightarrow CO$ (kJ/mol)	$O + O \rightarrow O_2$ (kJ/mol)	Error
Model 1	$23.13 \pm 1.52$	$58.01 \pm 7.27$	N/A	0.164
Model 2	$25.08 \pm 1.79$	N/A	N/A	0.159
Model 3	$29.08 \pm 2.20$	$55.90 \pm 4.36$	N/A	0.152
Model 4	$28.14 \pm 2.08$	$59.12 \pm 4.15$	$21.20 \pm 2.74$	0.128
Model 5	$27.36 \pm 2.11$	$58.23 \pm 4.93$	$23.92 \pm 3.15$	0.114
Model 6	$28.63 \pm 2.62$	$53.36 \pm 5.69$	$26.26 \pm 3.09$	0.105

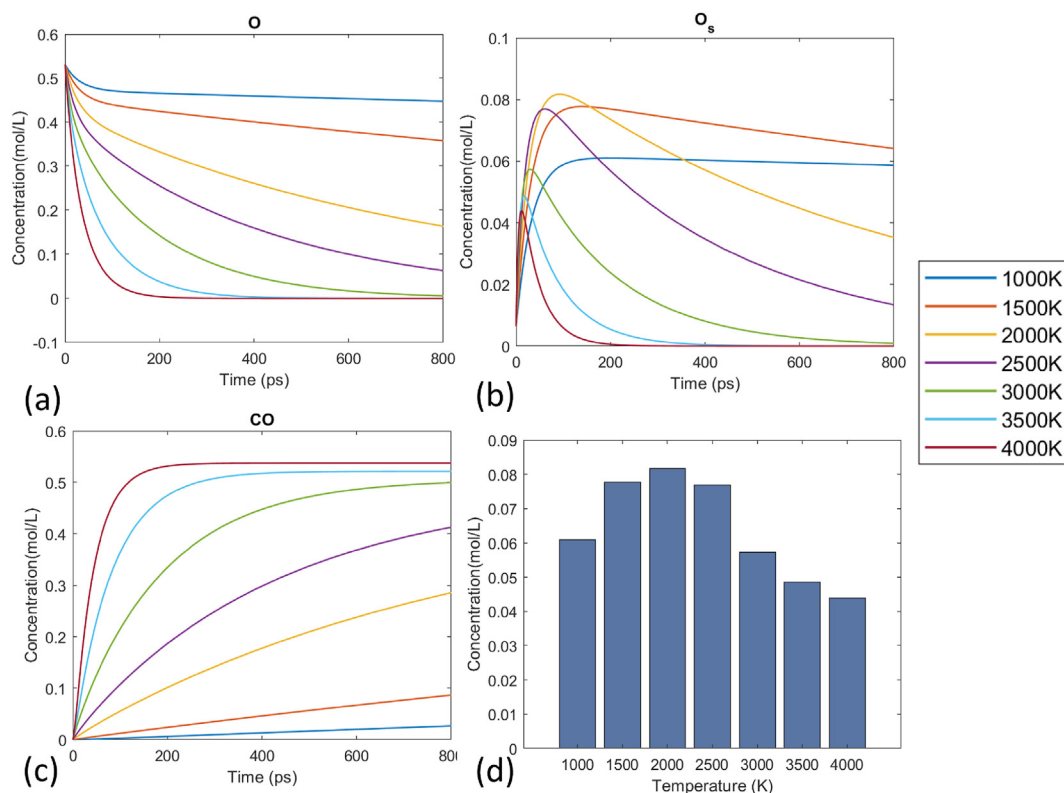
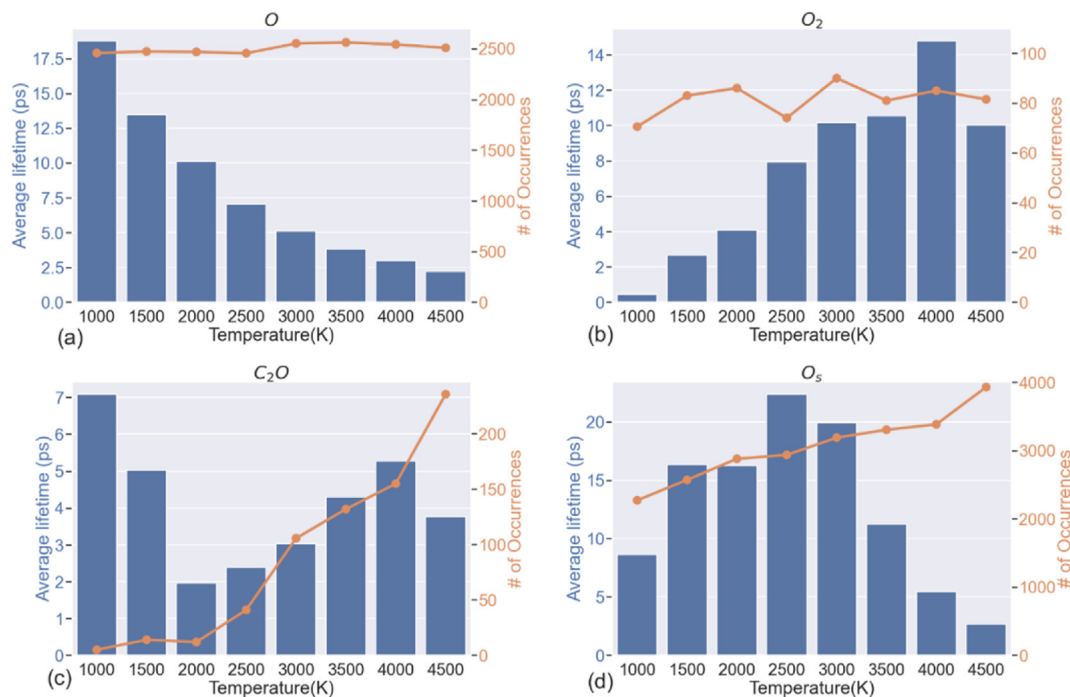


Fig. 9. (a–c) The predicted concentration of O,  $O_s$  and CO for CF as function of time by Model 5 for the oxidation of CF. (d) The predicted highest peak of  $O_s$  species evolution curves by Model 5 for the oxidation of CF.

of the initial oxygen having reacted to CO: there is little  $O_2$ ,  $CO_2$ ,  $O_s$  and  $C_xO$  remaining. Similar to  $O_2$ , the concentration of  $CO_2$  at high temperature increases initially and then decreases indicating the decomposition from  $CO_2$  to O and CO, which corresponds well with the analysis of average lifetime of  $CO_2$ . As shown in Fig. 7, the

concentration of  $O_s$  also increases at first and then decreases. At low temperature, the number of  $O_s$  increases showing that oxygen atom tends to adsorb on the fiber surface and not be reactive, which is also indicated by the nearly constant number of  $O_s + O$  as function of time; we discuss the long-time evolution below. At high



**Fig. 10.** (a–d) The average lifetime (blue bar) and occurrences (orange line) of O, O<sub>2</sub>, C<sub>2</sub>O and O<sub>s</sub> at from 1000 K to 4500 K during the oxidation simulation of amorphous carbon char. (A colour version of this figure can be viewed online.)

temperature, O<sub>s</sub> is initially adsorbed on the surface then reacts with other atoms or desorbs from the fiber surface, both of which can lead to the decrease of the number of O<sub>s</sub> after the peak. The total number of O<sub>s</sub> + O atoms decreases with increasing temperature, showing that oxygen atom tends to react with other atoms and transform to other molecules at high temperature. Another interesting aspect is that the highest concentrations of these intermediate molecules are not at the highest temperature; the peaks of concentration for O<sub>2</sub>, CO<sub>2</sub> and O<sub>s</sub> are 3500 K, 3000 K and 2000 K, respectively.

By fitting the six models, we obtain the reaction constants of each reaction model at each temperature. By fitting the reaction constants at different temperatures, we find that the computed reaction constants for all of the species that have substantial concentrations follow the Arrhenius equation, as expected. For species with very low concentrations, and hence few reactions, the data is too noisy to perform a quantitative analysis. The reactions for which Arrhenius fits can be made yield estimates of the activation energy that are consistent among the various models, as shown in Fig. 8. It should be noted that the reaction rates at 4500 K are not included for Model 1, 2 and 4 because of poor fitting; the error at 4500 K is 2–3 times larger than the value at other temperatures. We found that the three important reactions, (a)  $O + (s) \rightarrow O_s$  (b)  $C + O \rightarrow CO$ , and (c)  $O + O \rightarrow O_2$ , follow the Arrhenius equation. The activation energies with the error bars for the three reactions are listed in Table 2. Although, the six models have different systems of equations of varying complexity, we find the activation energies of these three reactions obtained from the Arrhenius fitting are consistent with each other, which indicates that these three reactions are significant in all the different models. The activation energy for oxygen adsorption  $O + (s) \rightarrow O_s$  is similar with that for the oxygen molecule generation  $O + O \rightarrow O_2$  and the activation energy for carbon oxidation  $C + O \rightarrow CO$  is around 57 kJ/mol.

In addition, the error of each model, as defined by Eq. (5), is shown in Table 2. It is not surprising that the error decreases from Model 1–6 with the increasing complexity. Although Model 2 has

same number of reactions as Model 1, reaction 15 in Model 2 considers both O and O<sub>s</sub> which decreases the predicted error. Models 3–6 have smaller errors due to the larger number of fitting parameters in the system of reaction equations. Since Model 5 has the least error of Models 1–5, none of which consider C<sub>x</sub>O explicitly, we use this model to predict the species change in a longer timer scale up to 800 ps (see Fig. 9 a-c). As is expected, the O is consumed much faster at high temperature than at low temperature. In addition, almost all O transform to CO at 3500 K and 4000 K. For the other temperatures, the concentration of CO still increases, and more time is needed to completely deplete the O. For all temperatures except 1000 K, the concentration of O<sub>s</sub> increases first and then gradually decreases. And, as shown Fig. 9(d), the highest peak of O<sub>s</sub> occurs at 2000 K predicted by Model 5.

### 3.2. Oxidation of carbon char

Compared with CF model, the char model has larger surface area, increasing the reaction rates at the same temperature. Also, the larger surface area enables most of O to be transformed to O<sub>s</sub> and adsorbed on the char surface decreasing the lifetime of O. Fig. 10(a–d) shows the average lifetime (blue bar) and occurrences (orange line) of O, O<sub>2</sub>, C<sub>2</sub>O and O<sub>s</sub> for amorphous carbon char at from 1000 K to 4500 K during the oxidation simulation. As shown in Fig. 10(a), the lifetime of the oxygen atoms decreases with increasing temperature, which is similar to the result of the oxidation CF. However, the overall lifetime of oxygen in amorphous carbon char simulation is smaller than in the CF fiber oxidation. Although the initial oxygen concentrations are very similar, char has a much larger surface area than the CF (2628 vs 646 nm<sup>2</sup>) by the estimation of the surface mesh. Therefore, we expect the reaction rate on the surface of char to be larger than on the surface of the CF. As shown in Fig. 10(b), the average lifetime of O<sub>2</sub> also increases from 1000 K to 4000 K and then decreases from 4000 K to 4500 K. Compared with CF oxidation simulation, O<sub>2</sub> has a longer lifetime and a much smaller occurrence in the char oxidation simulation.

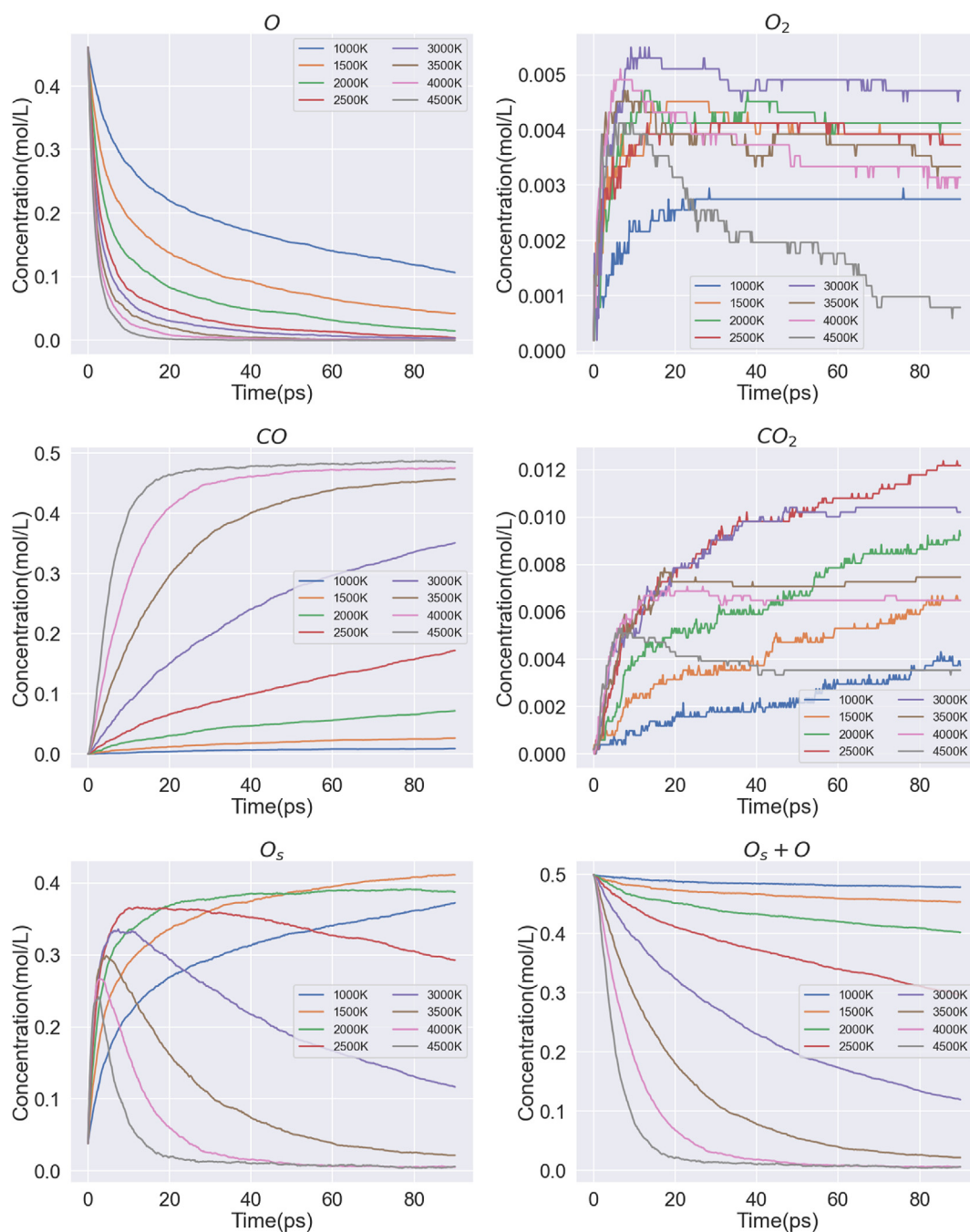


**Fig. 11.** The concentration of O, O<sub>2</sub>, CO, CO<sub>2</sub>, O<sub>s</sub> and (O<sub>s</sub> + O) as function of time during the oxidation simulation of amorphous carbon char. (A colour version of this figure can be viewed online.)

Fig. 10(c) shows the occurrence of C<sub>2</sub>O increases from 1000 to 4500K and the average lifetime of C<sub>2</sub>O in char oxidation is larger than in CF oxidation and the occurrence also increases with the increase of temperature. Fig. 10(d) shows the average lifetime of O<sub>s</sub> has its largest value, over 20 ps, at 2500 K. This lifetime value of O<sub>s</sub> in the char simulation is larger than in the CF simulation at the same temperature. Since the total number of oxygen atoms in char oxidation is only about one-third of the number in the fiber simulation, most of species undergo fewer reactions in the char oxidation than in the fiber simulation at the same temperature. However, the occurrence of O<sub>s</sub> is higher in the char simulation at low temperature because of its large surface area.

Fig. 11 shows the change in the concentration of the major species as a function of time in the amorphous carbon char oxidation. As in the case of the CF oxidation, the consumption rate of atomic oxygen and the generation rate of CO increase with increasing temperature. However, due to the smaller system and larger surface area of char, the slope of O and CO curves are steeper than in CF oxidation, indicating the higher reaction rate. Moreover, the curves of O<sub>2</sub> and CO<sub>2</sub> are also similar with those in the CF simulation: they increase with increasing temperature and then decrease at high temperature. Similar to the CF oxidation, the curve of O<sub>s</sub> also increases with temperature and then decreases, indicating similar adsorption and desorption mechanisms. The total

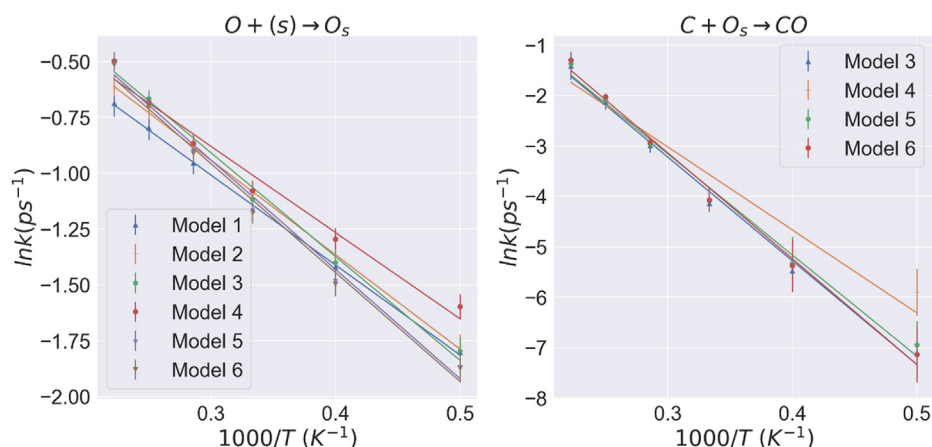


Fig. 12. Logarithm of the reaction rate against the inverse temperature for different reactions (a)  $O + (s) \rightarrow O_s$  (b)  $C + O_s \rightarrow CO$  for the oxidation of amorphous carbon char.

Table 3

The activation energy of reactions fitted from model 1 to model 6 and the prediction error of each model for the oxidation of amorphous carbon char.

	$O + (s) \rightarrow O_s$ (kJ/mol)	$C + O_s \rightarrow CO$ (kJ/mol)	Error
Model 1	$33.50 \pm 0.53$	N/A	0.421
Model 2	$35.28 \pm 0.48$	N/A	0.316
Model 3	$39.06 \pm 1.72$	$171.69 \pm 8.18$	0.301
Model 4	$32.69 \pm 2.43$	$157.85 \pm 14.34$	0.289
Model 5	$41.32 \pm 2.04$	$175.61 \pm 9.39$	0.278
Model 6	$41.35 \pm 2.21$	$184.74 \pm 8.67$	0.263

number of  $O_s + O$  atoms decreases with time, showing that atomic and adsorbed oxygen atoms react to form other molecules. The  $O_s + O$  curve reaches almost zero at around 50 ps in the char simulation at 4500 K. The completion time of  $O_s + O$  reaction is less than in the CF simulation. In conclusion, the reaction mechanisms in the char and fiber oxidation are similar but the reaction rate is larger in the char. Also, oxygen atoms tend to more readily adsorb on the surface of char due to the larger surface area compared with carbon fiber.

We use the same models to fit the oxidation curves of the amorphous carbon char. Moreover, since the concentration of the  $O_2$  and  $CO_2$  is low in the amorphous carbon char simulations, only  $O$ ,  $CO$  and  $O_s$  curves are used for fitting models. Similar to the fitting of CF model, we find these models fit well for temperatures ranging from 2000 K to 4500 K. The small number of reactions at 1000 K and 1500 K mean the rates have large uncertainties; these are not included in the fit. We found only two reactions, (a)  $O + (s) \rightarrow O_s$  (b)

$C + O_s \rightarrow CO$ , follow the Arrhenius law (see Fig. 12). The reason that the  $C + O$  reaction does not follow the Arrhenius law is that, as shown in Fig. 11, most oxygen atoms are adsorbed on the surface of char at the initial stage of the simulation. This leads the  $C + O_s \rightarrow CO$  to be the dominant reaction in the char oxidation. The activation energies of these two reactions and the fitting error of the models are listed in Table 3. The average activation energy of  $O + (s) \rightarrow O_s$  is 36 kJ/mol which is larger than the 27 kJ/mol value from the CF oxidation. The average activation energy of oxidation reaction  $C + O_s \rightarrow CO$  is around 172 kJ/mol, much larger than the activation energy of  $C + O \rightarrow CO$  in the CF oxidation. Moreover, Model 4 predicts a relatively low activation energy of the oxidation reaction, around 157 kJ/mol. Since the oxygen is adsorbed on the surface of the char, desorption of CO from the char surface also needs extra energy. That could contribute to the higher oxidation energy in the char simulation. Although the activation energy of reactions in char oxidation is higher, the pre-exponential factor is also higher. Therefore, the reaction rate in the char oxidation is higher than the reaction rate in the CF oxidation. Model 5 also has the lowest fitting error of Models 1–5. Therefore, it is also selected to predict the evolution of species up to 200 ps (see Fig. 13). The trends of prediction results are similar with the result of the CF oxidation. Also, the highest peak for  $O_s$  occurs at 2000 K for the char oxidation simulations ranging from 2000 K to 4500 K.

#### 4. Conclusions

Large-scale reactive MD simulations are performed for CF and amorphous carbon char. High fidelity models are constructed by

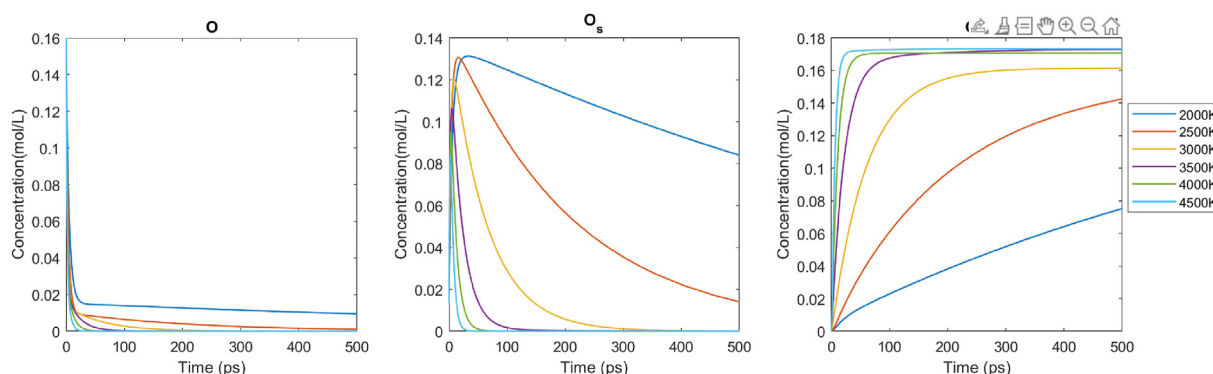


Fig. 13. The predicted concentration of  $O$ ,  $O_s$  and  $CO$  for CF as function of time by Model 5 for the oxidation of amorphous carbon char.

the combined kMC-MD and liquid quench methods, respectively. We demonstrate the ability of the CF and char models to simulate oxidation at high temperature using the MD method. We find that CO is the main product in the oxidation simulations of both CF and amorphous carbon, which is in agreement with the result of molecular beam experiments of CF [12]. In the oxidation process, we find that atomic oxygen tends to adsorb on the surface of the carbon fiber and char. Other species, most significantly  $O_2$ ,  $CO_2$  and  $C_xO$ , are also found in the oxidation process but at a much lower concentration than CO. The main species in the small molecules  $C_xO$  is  $C_2O$ , which is highly reactive and has a short lifetime compared with other species. Six reaction models are proposed. For CF oxidation simulation, the oxygen adsorption  $O + (s) \rightarrow O_s$ , carbon oxidation  $C + O \rightarrow CO$  and oxygen formation  $O + O \rightarrow O_2$  follow the Arrhenius law and have activation energies of 27 kJ/mol, 57 kJ/mol, and 24 kJ/mol, respectively. For the amorphous carbon oxidation simulations, the oxygen adsorption  $O + (s) \rightarrow O_s$  and carbon oxidation  $C + O_s \rightarrow CO$  follows the Arrhenius law and have average activation energies 38 kJ/mol and 172 kJ/mol, respectively. Compared with the CF oxidation, the carbon atoms of char react with adsorbed oxygen rather than atomic oxygen, which is more stable, resulting the higher activation energy of char oxidation. Moreover, the long-time evolution of the concentration of each is also predicted for both CF and amorphous char using the lowest error model. Overall, we have demonstrated the great potential of MD models for the simulation of oxidation of carbon fiber and amorphous carbon. These models can provide insights into the reaction mechanism that take place during the oxidation process. The MD simulations combined with high-fidelity atomic carbon models and the analytic mathematical model presented here not only shows the evolution of species at the initial state of oxidation but also increases the understanding of the oxidation mechanism at the initial state of CF and char. Moreover, the method presented here shows that the predictive tools have the potential to evaluate and analyze the material's response under extreme conditions, which is often difficult experimentally.

### CRediT authorship contribution statement

**Linyuan Shi:** Methodology, Software, Investigation, Writing – original draft, Visualization. **Marina Sessim:** Assistance and discussion of research methods and results, Writing – review & editing. **Michael R. Tonks:** Conceptualization, Resources, Writing – review & editing, Supervision. **Simon R. Phillpot:** Conceptualization, Resources, Writing – review & editing, Supervision, Data curation.

### Declaration of competing interest

The authors declare that they have no known competing financial interests or personal relationships that could have appeared to influence the work reported in this paper.

### Acknowledgments

This work was supported by the Early-Stage Innovations (ESI) NASA Grant 80NSSC18K0250. We are grateful to Joshua Monk for valuable discussions, and we thank Dr. Alexander Stukowski from the *Ovito* team for a valuable discussion about identifying carbon fiber surface atoms.

### Appendix A. Supplementary data

Supplementary data to this article can be found online at <https://doi.org/10.1016/j.carbon.2021.09.038>.

### References

- [1] C. Park, Calculation of stagnation-point heating rates associated with Stardust vehicle, *J. Spacecraft Rockets* 44 (2007) 24–32, <https://doi.org/10.2514/1.15745>.
- [2] K.A. Trick, T.E. Saliba, Mechanisms of the pyrolysis of a carbon/phenolic of phenolic composite resin, [https://doi.org/10.1016/0008-6223\(95\)00092-R](https://doi.org/10.1016/0008-6223(95)00092-R), 1995, 33, 1509–1515.
- [3] M. Stackpoole, S. Sepka, I. Cozmuta, D. Kontinos, Post-flight evaluation of Stardust sample return capsule forebody heatshield material, 46th AIAA Aerosp Sci Meet Exhib 1–7 (2008), <https://doi.org/10.2514/6.2008-1202>.
- [4] C. Szalai, E. Slimko, P. Hoffman, Mars science laboratory heatshield development, implementation, and lessons learned, *J. Spacecraft Rockets* 51 (2014) 1167–1173, <https://doi.org/10.2514/1.A32673>.
- [5] N.A.S.A. Final, Environmental Assessment for the Origins, Spectral Interpretation, Resource Identification, and Security-Regolith Explorer Mission, 2013.
- [6] A.J. Wise, D.K. Prabhhu, D.A. Saunders, C.O. Johnston, K.T. Edquist, Computational aerothermodynamic environments for the Mars 2020 entry capsule, *Jt Thermophys Heat Transf Conf* (2018) 1–14, <https://doi.org/10.2514/6.2018-3116>, 2018.
- [7] S. Poovathingal, E.C. Stern, I. Nompelis, T.E. Schwartzentruber, G.V. Candler, Nonequilibrium flow through porous thermal protection materials, Part II: oxidation and pyrolysis, *J. Comput. Phys.* 1 (2018) 1–15, <https://doi.org/10.1016/j.jcp.2018.02.043>.
- [8] M. Natali, J.M. Kenny, L. Torre, Science and technology of polymeric ablative materials for thermal protection systems and propulsion devices: a review, *Prog. Mater. Sci.* 84 (2016) 192–275, <https://doi.org/10.1016/j.pmatsci.2016.08.003>.
- [9] E.W. Ungar, Ablation Thermal Protection Systems: suitability of ablation systems to thermal protection depends on complex physical and chemical processes, *Science* 158 (1967) 740–744, 80.
- [10] S. Poovathingal, T.E. Schwartzentruber, V.J. Murray, T.K. Minton, G.V. Candler, Finite-rate oxidation model for carbon surfaces from molecular beam experiments, *AIAA J.* 55 (2017) 1644–1658, <https://doi.org/10.2514/1.J055371>.
- [11] K. Swaminathan-Gopalan, A. Borner, V.J. Murray, S. Poovathingal, T.K. Minton, N.N. Mansour, et al., Development and validation of a finite-rate model for carbon oxidation by atomic oxygen, *Carbon N Y* 137 (2018) 313–332, <https://doi.org/10.1016/j.carbon.2018.04.088>.
- [12] V.J. Murray, B.C. Marshall, P.J. Woodburn, T.K. Minton, Inelastic and reactive scattering dynamics of hyperthermal O and O<sub>2</sub> on hot vitreous carbon surfaces, *J. Phys. Chem. C* 119 (2015) 14780–14796, <https://doi.org/10.1021/acs.jpcc.5b00924>.
- [13] J. Lachaud, N.N. Mansour, Porous-material analysis toolbox based on OpenFOAM and applications, *J. Thermophys. Heat Tran.* 28 (2014) 191–202, <https://doi.org/10.2514/1.T4262>.
- [14] J. Lachaud, I. Cozmuta, N.N. Mansour, Multiscale Approach to ablation modeling of phenolic impregnated carbon ablators, *J. Spacecraft Rockets* 47 (2010) 910–921, <https://doi.org/10.2514/1.42681>.
- [15] D.E. Jiang, A.C.T. Van Duin, W.A. Goddard, S. Dai, Simulating the initial stage of phenolic resin carbonization via the ReaxFF reactive force field, *J. Phys. Chem.* 113 (2009) 6891–6894, <https://doi.org/10.1021/jp902986u>.
- [16] T. Qi, C.W. Bauschlicher, J.W. Lawson, T.G. Desai, E.J. Reed, Comparison of ReaxFF, DFTB, and DFT for phenolic pyrolysis. 1. Molecular dynamics simulations, *J. Phys. Chem.* 117 (2013) 11115–11125, <https://doi.org/10.1021/jp4081096>.
- [17] C.W. Bauschlicher, T. Qi, E.J. Reed, A. Lenfant, J.W. Lawson, T.G. Desai, Comparison of ReaxFF, DFTB, and DFT for phenolic pyrolysis. 2. Elementary reaction paths, *J. Phys. Chem.* 117 (2013) 11126–11135, <https://doi.org/10.1021/jp408113w>.
- [18] T.G. Desai, J.W. Lawson, P. Keblinski, Modeling initial stage of phenolic pyrolysis: graphitic precursor formation and interfacial effects, *Polymer (Guildf)* 52 (2011) 577–585, <https://doi.org/10.1016/j.polymer.2010.11.018>.
- [19] S. Poovathingal, T.E. Schwartzentruber, S.G. Srinivasan, A.C.T. Van Duin, Large scale computational chemistry modeling of the oxidation of highly oriented pyrolytic graphite, *J. Phys. Chem.* 117 (2013) 2692–2703, <https://doi.org/10.1021/jp3125999>.
- [20] X. Huang, Fabrication and properties of carbon fibers, *Materials (Basel)* 2 (2009) 2369–2403, <https://doi.org/10.3390/ma2042369>.
- [21] D.H. Wang, J.J. Hao, X.Q. Xing, G. Mo, Y. Gong, C.X. Lü, et al., Characterization of the nanopore structures of PAN-based carbon fiber precursors by small angle X-ray scattering, *Chin. Phys. C* 35 (2011) 870–874, <https://doi.org/10.1088/1674-1137/35/9/016>.
- [22] O. Paris, D. Loidl, H. Peterlik, Texture of PAN- and pitch-based carbon fibers, *Carbon N Y* 40 (2002) 551–555, [https://doi.org/10.1016/S0008-6223\(01\)00139-7](https://doi.org/10.1016/S0008-6223(01)00139-7).
- [23] S. Desai, C. Li, T. Shen, A. Strachan, Molecular modeling of the microstructure evolution during carbon fiber processing, *J. Chem. Phys.* 147 (2017), <https://doi.org/10.1063/1.5000911>.
- [24] L. Shi, M. Sessim, M.R. Tonks, S.R. Phillpot, Generation and characterization of an improved carbon fiber model by molecular dynamics, *Carbon N Y* 173 (2021) 232–244, <https://doi.org/10.1016/j.carbon.2020.11.011>.
- [25] R. Ranganathan, S. Rokkam, T. Desai, P. Keblinski, Generation of amorphous carbon models using liquid quench method: a reactive molecular dynamics study, *Carbon N Y* 113 (2017) 87–99, <https://doi.org/10.1016/>

- j.carbon.2016.11.024.
- [26] M. He, K. Joshi, L.V. Zhigilei, Theory Computational study of the effect of core – skin structure on the mechanical properties of carbon nanofibers, *J. Mater. Sci.* 56 (2021) 14598–14610, <https://doi.org/10.1007/s10853-021-06221-5>.
- [27] E.S. Penev, V.I. Artyukhov, B.I. Yakobson, Basic structural units in carbon fibers : atomistic models and tensile behavior, *Carbon N Y* 85 (2015) 72–78, <https://doi.org/10.1016/j.carbon.2014.12.067>.
- [28] K. Joshi, M.I. Arefev, L.V. Zhigilei, Generation and characterization of carbon fiber microstructure in atomistic simulations, *Carbon N Y* 152 (2019) 396–408, <https://doi.org/10.1016/j.carbon.2019.06.014>.
- [29] M. Guerrero, M.P. Ruiz, M.U. Alzueta, R. Bilbao, A. Millera, Pyrolysis of eucalyptus at different heating rates : studies of char characterization and oxidative reactivity, <https://doi.org/10.1016/j.jaap.2004.12.008>, 2005, 74, 307–314.
- [30] S. Plimpton, Fast parallel algorithms for short–range molecular dynamics, *J. Comput. Phys.* 117 (1995) 1–19.
- [31] S.L. Mayo, B.D. Olafson, W.A. Goddard, DREIDING: a generic force field for molecular simulations, *J. Phys. Chem.* 94 (1990) 8897–8909.
- [32] A.I. Jewett, Z. Zhuang, J.-E. Shea, Moltemplate a coarse-grained model assembly tool, *Biophys. J.* 104 (2013) 169a.
- [33] K. Chenoweth, A.C.T. van Duin, W.A. Goddard, ReaxFF reactive force field for molecular dynamics simulations of hydrocarbon oxidation, *J. Phys. Chem.* 112 (2008) 1040–1053, <https://doi.org/10.1021/jp709896w>.
- [34] X. Xing, X. Niu, Y. Liu, C. Yang, S. Wang, Y. Li, et al., In-depth understanding on the early stage of phenolic resin thermal pyrolysis through ReaxFF-molecular dynamics simulation, *Polym. Degrad. Stabil.* 186 (2021), <https://doi.org/10.1016/j.polymdegradstab.2021.109534>.
- [35] Y.Y. Zhang, Q.X. Pei, X.Q. He, Y.W. Mai, A molecular dynamics simulation study on thermal conductivity of functionalized bilayer graphene sheet, *Chem. Phys. Lett.* 622 (2015) 104–108, <https://doi.org/10.1016/j.cplett.2015.01.034>.
- [36] B.D. Jensen, K.E. Wise, G.M. Odegard, The effect of time step, thermostat, and strain rate on ReaxFF simulations of mechanical failure in diamond, graphene, and carbon nanotube, *J. Comput. Chem.* 36 (2015) 1587–1596, <https://doi.org/10.1002/jcc.23970>.
- [37] A. Stukowski, Visualization and analysis of atomistic simulation data with OVITO—the Open Visualization Tool, *Model. Simulat. Mater. Sci. Eng.* 18 (2010), 015012, <https://doi.org/10.1088/0965-0393/18/1/015012>.
- [38] L. Martinez, R. Andrade, E.G. Birgin, J.M. Martinez, PACKMOL: a package for building initial configurations for molecular dynamics simulations, *J. Comput. Chem.* 30 (2009) 2157–2164.
- [39] D.V. Ilyin, W.A. Goddard, J.J. Oppenheim, T. Cheng, First-principles–based reaction kinetics from reactive molecular dynamics simulations: application to hydrogen peroxide decomposition, *Proc. Natl. Acad. Sci. U.S.A* (2018), 201701383, <https://doi.org/10.1073/pnas.1701383115>.